Research in Astronomy and Astrophysics, 22:035012 (7pp), 2022 March https://doi.org/10.1088/1674-4527/ac47a8

Method of Separating Cosmic-Ray Positrons from Electrons in the DAMPE Experiment

Hao-Ting Dai[1,2], Jing-Jing Zang[3,4], Ying Wang[1,2], Chuan-Ning Luo[4], Yun-Long Zhang[1,2], Zhi-Yong Zhang[1,2], Yi-Feng Wei[1,2], Li-Bo Wu[1,2,5], Cheng-Ming Liu[1,2], Cong Zhao[1,2], Xiao-Lian Wang[1,2], Zi-Zong Xu[1,2], and Guang-Shun Huang[1,2]
[1] State Key Laboratory of Particle Detection and Electronics, University of Science and Technology of China, Hefei 230026, China; ylzhang@ustc.edu.cn, weiyf@ustc.edu.cn, hgs@ustc.edu.cn
[2] Department of Modern Physics, University of Science and Technology of China, Hefei 230026, China
[3] School of Physics and Electronic Engineering, Linyi University, Linyi 276000, China
[4] Key Laboratory of Dark Matter and Space Astronomy, Purple Mountain Observatory, Chinese Academy of Sciences, Nanjing 210023, China
Received 2021 August 24; revised 2021 December 8; accepted 2021 December 20; published 2022 February 18

Abstract

A method of identifying positron/electron species from the cosmic rays was studied in the DArk Matter Particle Explorer (DAMPE) experiment. As there is no onboard magnet on the satellite, the different features imposed by the geomagnetic field on these two species were exploited for the particle identification. Application of this method to the simulation of on-orbit electrons/positrons/protons and the real flight data proves that separately measuring the CR positrons/electrons with DAMPE is feasible, though limited by the field of view for the present observation data. Further analysis on the positron flux with this method can be expected in the future.

Key words: (ISM:) cosmic rays – magnetic fields – (cosmology:) dark matter

1. Introduction

Positrons, as a species of elementary particles, were first discovered by C. D. Anderson, in cosmic-ray (CR) tracks in a vertical Wilson chamber (Anderson 1933). The abundance and energy measurements of positrons in cosmic-rays were first made in 1960s (De Shong et al. 1964; Fanselow et al. 1969). At that time, theoretical studies pointed out that a measurement of positron-to-electron ratio would be of great help to determine the origin of CR positrons and electrons (Ginzburg & Syrovatsky 1961). From then on, people have kept trying to send instruments into the sky to measure CR positrons.

More recently, the PAMELA experiment reported their result on the ratio up to 100 GeV and pointed out that the positron fraction ($e^+/(e^+ + e^-)$) might reach its minimum at ~10 GeV and begin to increase as the energy goes higher (Adriani et al. 2009, 2010). This observation was confirmed afterwards by Fermi-LAT (Ackermann et al. 2012) and AMS-02 (Accardo et al. 2014; Aguilar et al. 2019).

The origin of CR positrons is now generally acknowledged as secondary production in the interstellar medium: the primary CR nuclei propagate in space and interact with interstellar gas, during which pions are produced and then decay into neutrinos, electrons and positrons. However, the hardening feature in the positron spectrum compared to CR electrons is not fully accounted by this mechanism. It remains a puzzle today and is called "the excess of positrons at high energy." The possible source of positron flux excess may be ascribed to pulsars, CRs interacting with giant molecular clouds, or dark matter (Fan et al. 2010; Porter et al. 2011; Aguilar et al. 2019).

For the DArk Matter Particle Explorer (DAMPE), it is hard to distinguish positrons from electrons, as the instrument does not have an onboard magnet, and the behavior of positrons in the detectors is almost the same as that of electrons. However, in the last century, pioneers started trying to use the geomagnetic field to separate the two species (Mueller & Tang 1987). With the only difference being the sign of charge, the identification of positrons and electrons would be possible with some magnetic effects, as the geomagnetic field bends propagating positrons and electrons toward opposite directions. Fermi-LAT separately measured CR positrons and electrons based on this idea (Ackermann et al. 2012), and became the first to claim a continuing positron excess up to ~200 GeV. In light of this, we simulated the different "horizons" of cosmic ray positrons and electrons, and used this difference to select positrons while eliminating electrons (or vice versa). The application of this method to a simulated data sample and the flight data demonstrates that the separation of these two species is feasible with the DAMPE experiment.

2. DAMPE Instrument

DAMPE is a scientific satellite, which was launched into a Sun-synchronous orbit at an altitude of ~500 km from the Jiuquan Satellite Launch Center at the end of 2015 (Chang et al. 2017). It has three main scientific objectives: searching

[5] Libo Wu is now at Gran Sasso Science Institute (GSSI), Via Iacobucci 2, I-67100 L'Aquila, Italy.

for the signals of dark matter particles (Lu et al. 2014), understanding the mechanisms of cosmic ray acceleration in astrophysical processes (An et al. 2019), and studying Galactic and extragalactic sources of γ-ray emission (Xu et al. 2018). DAMPE has been operating well since its launch and will continue the observation for the three scientific objectives.

The whole spectrometer of DAMPE consists of four sub-detectors. From top to bottom, there are a Plastic Scintillator Detector (PSD) (Ding et al. 2019), a Silicon-Tungsten tracKer-converter (STK) (Azzarello et al. 2016), a Bismuth Germanium Oxide (BGO) calorimeter (Zhang et al. 2016), and a NeUtron Detector (NUD) (Ming et al. 2016). The PSD, which is composed of two orthogonal layers of plastic scintillator strips with dimensions of $884 \times 28 \times 10$ mm, is designed to measure the charge of incident particles, on the basis of the proportionality between Z^2 (Z is the number of unit of charge that the particle carries) and the ionization energy loss (Ding et al. 2019). The STK has a six-layer structure, with each layer made of two sub-layers of orthogonally arranged silicon microstrips. The STK enables the reconstruction of particle directions. The BGO calorimeter contains 14 layers of BGO crystals, making more than 31 radiation lengths and $\sim$1.6 nuclear interaction lengths on axis. Each crystal layer is composed of 22 BGO crystal bars that are arranged in an orthogonal way between adjacent layers. The BGO calorimeter measures the energy deposited in the scintillation crystals, but the crystals arranged in such a way are able to give information on the spatial profile of hadronic and electromagnetic showers developed in it. Moreover, the BGO calorimeter provides the triggers for the data acquisition system (Zhang et al. 2019) and the seed for reconstructing the track in the STK sub-detector. The NUD is made of four boron-loaded plastic scintillators, each with a set of photomultiplier tubes and related electronics. It provides additional electron/hadron discrimination, further increases the proton rejection at TeV energies. More details about DAMPE can be found in Chang et al. (2017).

3. Geomagnetic Environment and the East–West Effect

The geomagnetic field, though has a north pole and a south pole, is much more complicated than a dipole magnetic field. Modeling the magnetic environment for a computer simulation is indispensable for the study of behavior of cosmic ray positrons and electrons in the field. The International Geomagnetic Reference Field (IGRF) is a series of mathematical models of the field, updated every five years by the International Association of Geomagnetism and Aeronomy (IAGA). This high-precision model is a product of IAGA Working Group V-MOD (formerly V-8), which is supported by many magnetic field modelers and organizations involved in operating magnetic survey satellites, observatories, magnetic survey programmes and World Data Centers. It is used widely in studies of the Earth's deep interior, its crust and its ionosphere and magnetosphere.

The IGRF gives a standard mathematical description of the Earth's main field and its annual rate of change (which is commonly called "secular variation"). In source-free regions at the Earth's surface and above, the main field, with sources internal to the Earth, is the negative gradient of a scalar potential V that can be represented by a truncated series expansion:

$$V(r,\theta,\phi,t) = a\sum_{n=1}^{N}\sum_{m=0}^{n}\left(\frac{a}{r}\right)^{n+1} \times [g_n^m(t)\cos(m\phi) + h_n^m(t)\sin(m\phi)]P_n^m(\cos\theta) \quad (1)$$

in spherical coordinates. The series is truncated at degree $N = 13$, with $a = 6371.2$ km being the geomagnetic conventional Earth's mean reference radius and $P_n^m(\cos\theta)$ the Schmidt quasi-normalized associated Legendre functions. The Gauss coefficients g_n^m, h_n^m are functions of time and are computed from candidate sets of coefficients produced by the participating members of V-MOD, who are involved in collecting and disseminating magnetic field data from satellites, observatories and surveys around the world.

The 12th generation of the model (IGRF-12) was adopted for this analysis. The model was finalized in 2014 December, providing a main field model for epoch 2015 and a predicted rate of change for 2015–2020 (Thébault et al. 2015).

The dynamics of radiation in the geomagnetic field has been studied from 1960s (Roederer 1970). For studies that involve physical mechanisms governing the Earth's radiation environment, Carl E. McIlwain established a coordinate system (McIlwain 1966) to accurately present the results. The McIlwain L-parameter describes a set of the Earth's magnetic field lines, in particular those which cross the Earth's magnetic equator at a number of Earth-radii equal to the L-value. Magnetically equivalent positions (from the standpoint of the incident charged particle) around the world will by definition have the same McIlwain L values. The different behavior between CR positrons and electrons are most prominent around the regions with smaller McIlwain L values. In Figure 1, the black band represents a chosen region with restricted L values in the range (1.00, 1.14). Cosmic rays detected in positions with similar L value have similar geomagnetic features. When getting out of the band, the L value is larger than the range and starts to increase more rapidly (with theoretically no upper limit) as the position gets farther from it. As for the tiny hole within the band, though the L values are smaller, the data collected with these L values are also limited. In this paper, the analysis method is applied to the data detected over the region with $L \in (1.00, 1.14)$.

The propagation of cosmic rays in the geomagnetic field can be simulated using a tracer code developed by Smart and Shea (Smart & Shea 2000). This tracer method has been integrated

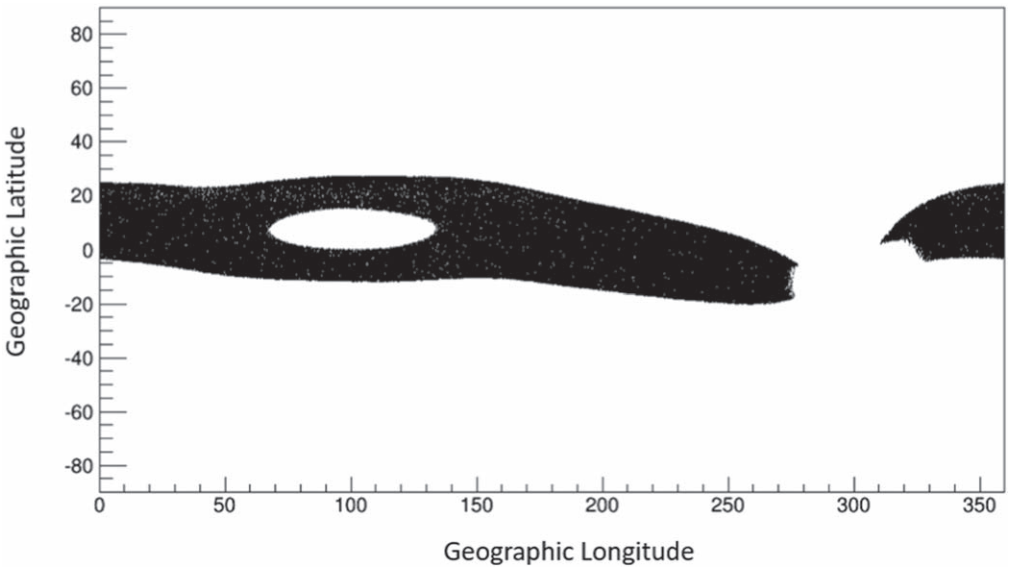

Figure 1. The region of McIlwain L value between 1.00 and 1.14 for the orbit at an altitude of 500 km. The blank region is of L either larger or smaller than the range (1.00, 1.14).

into the simulation of the DAMPE experiment. For convenience, the propagation is traced backward from the detected location. It back traces particles that hit the detectors from different directions, and computes their trajectories before they are detected. Generally, the trajectory of a charged particle undergoes increased geomagnetic bending as the particle energy decreases. In the simulation, particles that had reached 10 Earth radii before they were detected are called "escaped," as they had come from very far from the Earth and should be cosmic rays of Galactic origin. Particles with a trajectory that eventually collides with the Earth are not considered cosmic ray particles. In the simulation there are some particles that are back traced for a time long enough while neither escaping from nor intersecting the Earth (maybe captured by the field). They are either not taken as cosmic rays. This method for simulating a real on-orbit detection of cosmic rays is confirmed valid in a previous work of DAMPE (Dai et al. 2020).

In the simulation, every particle detected (reconstructed as an event) by DAMPE is back traced the way described above. The positron events that are simulated as "escaped" are observed as arriving from some characteristic directions from DAMPE's point of view. Figure 2 is the distribution of directions (represented in polar coordinates) from which cosmic ray positrons (with energy 12–13 GeV) arrive at DAMPE when the satellite is over the region of $L \in (1.00,\ 1.14)$. The radial coordinate represents the zenith angle that varies from 0° to 180°, indicating the particle comes upward or downward. Particles coming upward from the Earth center have radial coordinate as 0°, and particles flying right downward have radial coordinate as 180°. The angular coordinate represents the azimuth angle that varies from 0° to 360°, indicating whether the particle comes from the north, the south, the east, or the west. We can see that cosmic ray positrons are more likely coming from the west than from the east, and a very large area in the plane polar coordinates has no allowed arrival direction for positrons. This blank area is due to the Earth blocking cosmic rays from behind, thus leading to a shadow of it. It is to be noted that DAMPE does not simulate particles that hit the detectors upward, so there are no particles with zenith angle less than 90° to be back traced. Therefore it is only a technical issue that the boundary between the blue points and the shadow is located exactly at 90° in the west. The real boundary of the shadow should have smaller radial coordinates. Still, the shadow is not as round as the shape of the Earth, because the propagation of charged particles has been deviated by the geomagnetic field. In other words, the boundary can be called the "deviated horizon," since it is actually the boundary of the Earth, if you watch the sky via CR positrons rather than neutral particles. The golden dashed line in Figure 2 is the Earth's "horizon" in its original meaning. Neutral particles such as photons propagate with no bending so that the "horizon" is not deviated but a standard circle.

For CR electrons, it is the opposite: the horizon is deviated by the geomagnetic field toward the west, as the magnetic field bends electrons to the other side. Figure 3 draws the horizons together, to intuitively show the deviation of the two species.

In Figure 3, the horizons of the two species are deviated to different directions. The horizon of positrons is deviated to the east (as positrons are more likely coming from the west), while the horizon of electrons is deviated to the other side. Above the

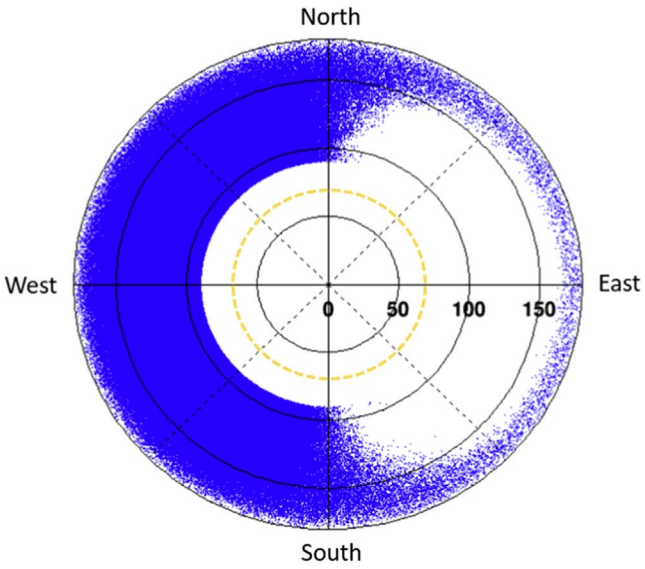

Figure 2. The reconstructed arrival directions of cosmic ray positrons (blue points) between 12 and 13 GeV, during observation over the region of McIlwain L value between 1.00 and 1.14 in the simulation. The radial coordinates represent the zenith angle of the arrival direction. Because the inner z-axis of DAMPE points to the Earth center, the particle coming from the Earth center has zenith as 0°. The boundary between the blue points and the blank caused by the Earth stops at 90° and cannot be smaller than it, because the simulation of the DAMPE experiment does not simulate particles coming upwards. The golden dashed line represents the shape of the Earth, which is at ∼68°, seen from DAMPE.

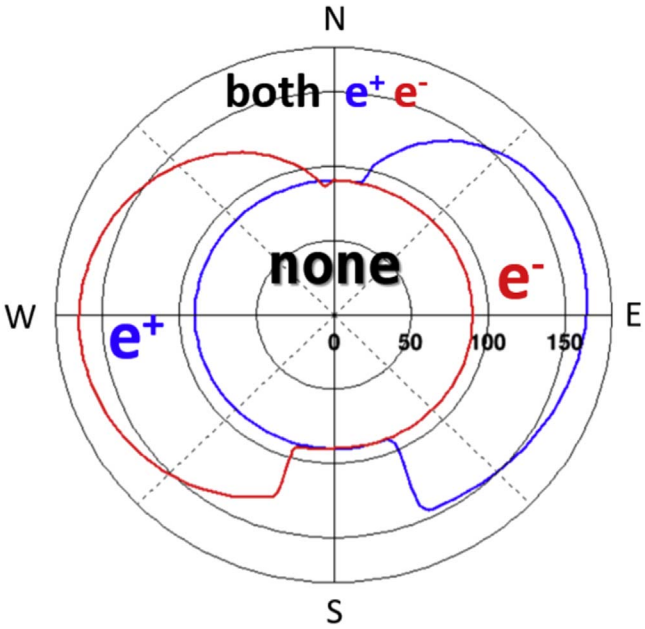

Figure 3. The deviated horizons of CR positrons and electrons. Above the positron horizon (larger radial coordinates than that of the blue boundary) are the directions from which CR positrons can arrive, and below are the directions blocked by the Earth. The red boundary stands for the horizon of CR electrons.

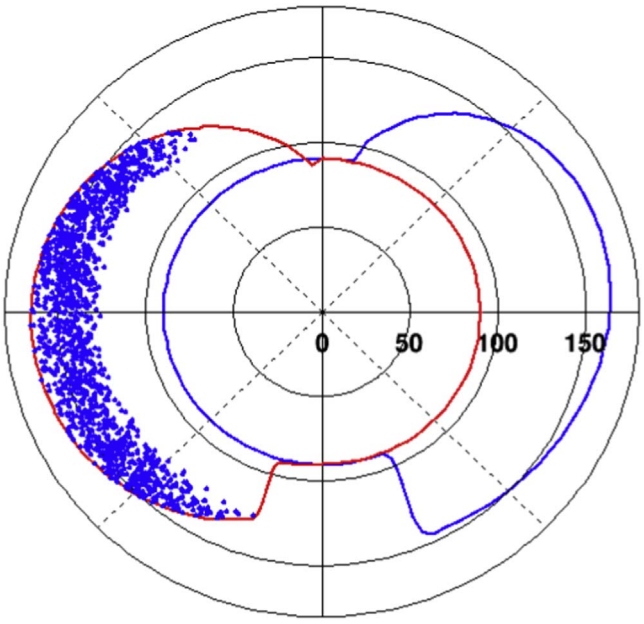

Figure 4. The selected events (blue points) from the data. They are above the positron horizon (blue line) and below the electron horizon (red line). For the positron horizon, the part below electron horizon is already out of the field of view of DAMPE for these azimuth angles so the selected data sample stops at some certain zenith angle and cannot touch the positron horizon.

positron (electron) horizon are the allowed arrival directions for positrons (electrons).

4. Data Analysis

4.1. Event Selection

It is now clear that there are some directions from which only CR positrons (or electrons) can arrive at DAMPE. For example, by selecting events that are above the positron horizon and below the electron horizon, the CR electrons are definitely excluded.

As stated in Section 3, the deviated horizons are related to the particle energy and the location where the DAMPE satellite is. To apply the above-mentioned idea, selecting a data sample with good energy reconstructions and good tracks is vital for this analysis. Based on the selection used for the combined $e^+ + e^-$ spectrum measurement with DAMPE (see detail in Ambrosi et al. 2017), the selection criteria applied here were optimized for lower energy events. The angular resolution of the reconstructed track is better than $0.^\circ3$ for particles above 10 GeV and better than $0.^\circ1$ above 100 GeV (Chang et al. 2017). The PSD sub-detector can give the information on the particle charge for eliminating heavier nucleus events.

Figure 4 shows the distribution of arrival directions of a selected sample of the experimental orbit data (from 2016 January to 2019 December): the selected events are well above

the positron horizon and below the electron horizon, which means there are no electrons. We find that the arrival directions are distributed next to the electron horizon (red boundary) while do not reach the positron horizon (blue boundary), because as the zenith angle gets smaller (closer to the blue boundary while below the red one), it gets out of the effective field of view of DAMPE, which is a combined result of the satellite observation mode and the event selection described above.

Note that DAMPE has always been operating in the survey mode since its launch, and this means that until now it has been "looking" with its field of view right toward the sky. However, the offsets between the two horizons are located at sidewards. At the energy 12–13 GeV, though at sidewards, some of the special directions for CR positrons are still within the field of view. When the energy goes higher, the special directions gradually fall out of the field of view and cannot be observed in survey mode.

The situation of selecting events above the electron horizon while below the positron horizon is alike, only with the allowed directions in the east. It will not be further developed in this article.

4.2. Result

For the selected experimental data (the blue points in Figure 4), there are still some proton background left. To give a measurement of CR positrons, the proton background has to be subtracted. The 3D imaging calorimeter can help us distinguish positron/electron events from protons. The cascade process of protons is hadronic interaction with the calorimeter while the cascade of positrons/electrons is electromagnetic. This fact leads to different behavior of protons from electrons/positrons, including the starting point of cascade process, energy deposition profile in the calorimeter, etc.

We can number the BGO layers in the calorimeter from top to bottom, and define the energy spread within the ith layer as the energy-weighted root-mean-square value of the deposition positions around the barycenter of energy (the same definition as in Ambrosi et al. 2017):

$$\mathrm{rms}_i = \sqrt{\frac{\sum_j (x_{j,i} - x_{c,i})^2 E_{j,i}}{\sum_j E_{j,i}}} \tag{2}$$

where the subscript j stands for the jth BGO bar in the ith BGO layer, and $x_{c,i}$ stands for the position of the barycenter of energy within the ith layer.

On the other hand, since the selected events first get into the PSD sub-detector and the STK sub-detector before the BGO calorimeter, the last layer where the particle still deposits energy in the BGO can be called the "tail layer," defined as the last layer that still contains more than 1% of the total energy that the particle deposits in the whole calorimeter. With the concept of "tail layer" and the layer rms in (2), we have the variable defined as below that can help distinguish the proton contamination in the selected sample:

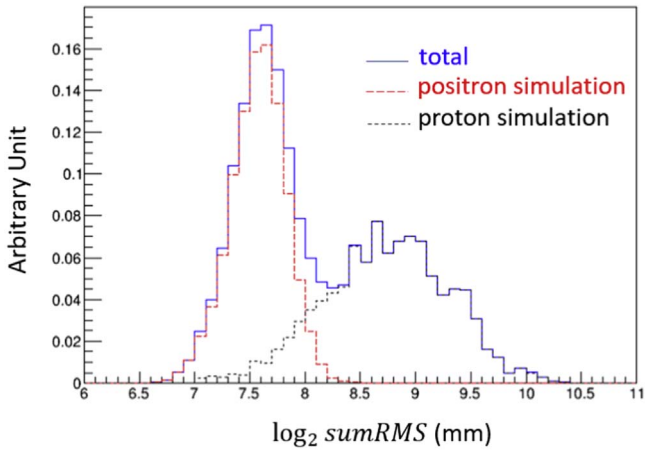

Figure 5. The distributions of positrons and protons on the variable defined in Equation (3). The two samples are separately simulated and selected, and drawn together with the sum of arbitrary mixing ratio between the two.

$$\log_2 \mathrm{sumRMS} = \log_2\left(\sum_{i=1}^{\text{tail layer}} \mathrm{rms}_i\right). \tag{3}$$

Through a selected sample of simulated positrons and a selected sample of simulated protons, we can see the positron/proton discrimination on this variable in Figure 5. The distribution of positrons and the distribution of protons are drawn together with the sum of the two. The distribution of positrons is located at smaller values of this variable than the distribution of protons. The behavior of electrons in the calorimeter is similar to positrons.

Besides, by further selecting events with energy deposition in the 14th layer (the last layer) <0.1% of the total energy in the calorimeter (this requirement considerably suppresses the proton background while passes the positron events), now we demonstrate how to subtract the proton contamination from our selected data sample.

In Figure 6, the signal and background distributions are each parameterized with a Gaussian, thus the number of signal events can be statistically estimated by integrating the fit functions. By varying the parameters of the Gaussians within ±3 times the uncertainty of the fit values, the maximum deviation of the calculated positron signals is 7%. The simulation of positrons confirms that Gaussian function deviates from positron signal distribution by less than 1%, which means the Gaussian choice is sufficient to obtain the number of signals at this level. By fixing the sigma parameter of the signal Gaussian to the value obtained by fitting the simulated positron sample, while setting other parameters free, the estimated positron fraction $e^+/(e^+ + e^-)$ at energy between

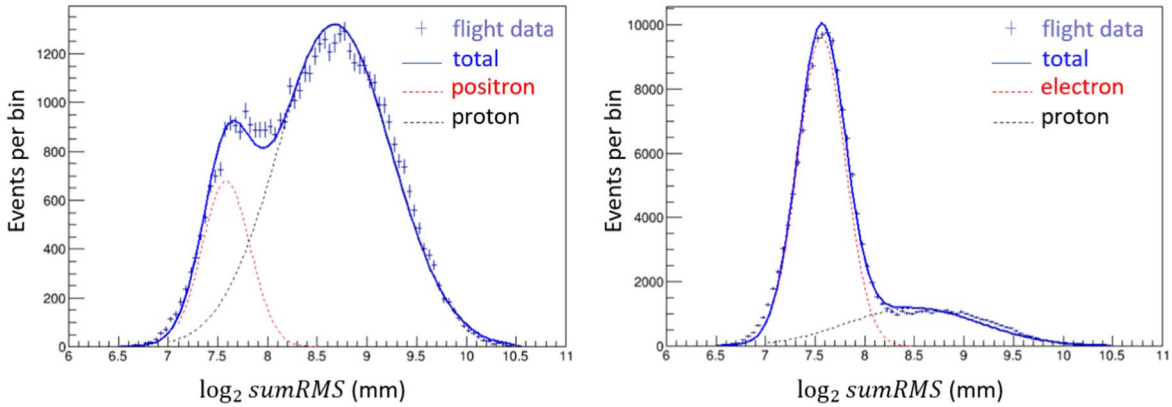

Figure 6. The logarithmic sumRMS distribution of the events below electron horizon (positron candidates with proton contamination) and below positron horizon (electron candidates with proton contamination). The two samples are of reconstructed energy between 12 and 13 GeV.

12 and 13 GeV is 7.7%, with uncertainty estimated (statistical and systematic uncertainties included) as 2%.

The fraction measurement given by AMS-02 at this energy is ∼5.6%, and reaches ∼6.3% over 20 GeV with slow increase (Accardo et al. 2014). However, the result given by Fermi-LAT is 9.4% at 22.4 GeV and increases as the energy goes higher (Ackermann et al. 2012). Fermi-LAT has no precise data below 20 GeV because of the limitation of its trigger mode. Within the uncertainty, the estimate of positron fraction with the method here agrees with the measurements given by other experiments.

5. Conclusion

DAMPE is a satellite-borne spectrometer without onboard magnets, which means that originally it was not designed to distinguish the sign of charge, and it could only measure CR electrons and positrons together. In order to separately measure the CR positrons, the different behavior that results from the geomagnetic field effect shed light on the identification of positrons. With an established model of the geomagnetic field, the possible incident directions of CR positrons and electrons are simulated by computing the particle's propagation trajectory in the field before it arrives at DAMPE. Because of the deflection during the propagation, the positron "horizon" and the electron "horizon" are found to both deviate from the original horizon of the Earth. There are some directions that are above the positron "horizon" while below the electron "horizon." Selecting events arriving from these directions can help us select CR positrons while definitely keep CR electrons excluded. The performance of the selection method is illustrated with application on the flight data, which demonstrates the feasibility of separately measuring CR positrons in the DAMPE experiment. Then the number of positron candidates should be determined after subtracting the proton contamination from the selected events within these constrained directions. The difference between proton shower and positron shower developed in the calorimeter can help us do it statistically.

Limited by the field of view of DAMPE in survey mode, the highest energy where we can apply the method for now is only about 20 GeV. The method may be applied for energies up to ∼200 GeV in the best case if DAMPE turns to "look" sidewards. In this article, the analysis of positrons between 12 and 13 GeV is performed to illustrate the method. We leave a positron flux measurement to the works in the future. In conclusion, the method is expected to be applicable for a measurement of positron spectrum when DAMPE changes its observation mode, or further, for other future space experiments that are not equipped with onboard magnets, like DAMPE. By using the geomagnetic effect, the upper bound of energy range should be limited by the strength of the field.

Acknowledgments

This work is supported by the Outstanding Youth Science Foundation of NSFC (Grant No. 12022503), the Joint Funds of the National Natural Science Foundation of China (Grant Nos. U1738208, U1738139, U1738135 and U1738207), the National Natural Science Foundation of China (Grant Nos. 11673021, 11705197, 11773085 and 11851302), the National Key Research and Development Program of China (Grant No. 2016YFA0400200), and Youth Innovation Promotion Association CAS (Grant No. 2021450).

References

Accardo, L., Aguilar, M., Aisa, D., et al. 2014, PhRvL, 113, 121101
Ackermann, M., Ajello, M., Allafort, A., et al. 2012, PhRvL, 108, 011103
Adriani, O., Barbarino, G., Bazilevskaya, G., et al. 2010, APh, 34, 1
Adriani, O., Barbarino, G. C., Bazilevskaya, G. A., et al. 2009, Natur, 458, 607
Aguilar, M., Ali Cavasonza, L., Alpat, B., et al. 2019, PhRvL, 122, 101101
Ambrosi, G., An, Q., Asfandiyarov, R., et al. 2017, Natur, 552, 63
An, Q., Asfandiyarov, R., Azzarello, P., et al. 2019, SciA, 5, eaax3793
Anderson, C. D. 1933, PhRv, 43, 491
Azzarello, P., Ambrosi, G., Asfandiyarov, R., et al. 2016, NIMPA, 831, 378

Chang, J., Ambrosi, G., An, Q., et al. 2017, APh, 95, 6
Dai, H. T., Zhang, Y. L., Zang, J. J., et al. 2020, ITNS, 67, 956
De Shong, J. A., Hildebrand, R. H., & Meyer, P. 1964, PhRvL, 12, 3
Ding, M., Zhang, Y.-P., Zhang, Y.-J., et al. 2019, RAA, 19, 47
Fan, Y.-Z., Zhang, B., & Chang, J. 2010, IJMPD, 19, 2011
Fanselow, J. L., Hartman, R. C., Hildebrad, R. H., & Meyer, P. 1969, ApJ, 158, 771
Ginzburg, V. L., & Syrovatsky, S. I. 1961, PThPS, 20, 1
Lu, T.-S., Dong, T.-K., & Wu, J. 2014, RAA, 14, 520
McIlwain, C. E. 1966, SSRv, 5, 585
Ming, H., Tao, M., Jin, C., et al. 2016, ChA&A, 40, 474
Mueller, D., & Tang, K.-K. 1987, ApJ, 312, 183
Porter, T. A., Johnson, R. P., & Graham, P. W. 2011, ARA&A, 49, 155
Roederer, J. G. 1970, Dynamics of Geomagnetically Trapped Radiation (Berlin: Springer)
Smart, D. F., & Shea, M. A. 2000, Final Report Grant , NAG5-8009, Tech. Rep., Center for Space Plasmas and Aeronomic Research, The University of Alabama in Huntsville
Thébault, E., Finlay, C. C., Beggan, C. D., et al. 2015, EP&S, 67
Xu, Z.-L., Duan, K.-K., Shen, Z.-Q., et al. 2018, RAA, 18, 27
Zhang, Y.-Q., Guo, J.-H., Liu, Y., et al. 2019, RAA, 19, 123
Zhang, Z., Wang, C., Dong, J., et al. 2016, NIMPA, 836, 98